eCSE09-10

Developing a multiscale continuum framework for exascale computing of fluids with microstructure

Chrysovalantis Tsigginos[1] and Charles Moulinec[1]

[1]Scientific Computing Department, STFC Daresbury Laboratory, Warrington WA4 4AD, United Kingdom

***Abstract*—A finite volume solver for micropolar fluids entitled CS_MICRO has been added within the framework of Code_Saturne, an open-source CFD software. A PISO-type algorithm was developed and implemented to handle the coupling of the discretized pressure, linear momentum and angular momentum equations of incompressible isotropic micropolar fluids. Extensions of the developed algorithm to compressible micropolar fluids and incompressible micropolar fluids with free surfaces were also developed and implemented in the new module. The new developments were validated against analytical and numerical benchmark cases, including channel flows, two-dimensional lid-driven cavity flows. Scalability tests conducted on ARCHER2 indicate that the developed module retains the excellent parallel performance of Code_Saturne.**

I. INTRODUCTION

Many natural and industrial processes involve fluids with microstructure, including but not limited to landslides, avalanches, lateral spreading, blood flows with clots, polymers, granular flows, liquid crystals, suspensions of rigid and/or deformable particles and even turbulent flows. For the accurate modeling of such fluids, the evolution of the microstructure must be taken into account. Classical continuum theories are unable to correctly predict the evolution of the material microstructure. In contrast, atom-based methods can predict the evolution of the microstructure with sufficient accuracy, but the enormous number of atoms involved in the calculations, typically in the order of trillions, renders those methods prohibited for the simulation of industrial-scale problems even on the largest existing supercomputers. Continuum theories that introduce additional degrees of freedom to model the evolution of the microstructure can bridge the gap between the computational accuracy of atom-based methods and the computational efficiency of continuum methods.

The simplest of such theories is the micropolar theory [3, 5] which material points (i.e., rigid bodies) carry three extra rigid directors (i.e., rotational degrees of freedom) in addition to the translational degrees of freedom of the classical continuum medium. The introduction of additional degrees of freedom renders the micropolar theory an excellent platform for the modeling of materials consisting of dumb-bell type molecules, cylindrical elements and rigid bodies of various shapes. In that regard, the micropolar theory can be applied to the modeling of non-conventional fluids such as blood [11, 10], granular fluids [12, 13], even flows with shear turbulence flows [15].

The significant increase in computational power witnessed with the development of Petascale and, lately, of Exascale systems has shifted the numerical modeling from being a verification tool of experimental procedures to a powerful tool that can be used directly in the design of new materials/processes or in the optimization of existing ones. Therefore, there is an increased demand for open-source software optimized for high performance systems. In that regard, Code_Saturne [1], an open-source computational fluid dynamics software, optimized for high performance systems [7] constitutes an ideal platform for the development of numerical solvers of such complex fluids.

The scope of this study is the development of an open-source finite volume solver entitled CS-MICRO build within Code_Saturne framework that solves the transport equations of micropolar fluids which will also form the basis for further developments within the continuum modeling of fluids with microstructure.

II. MICROPOLAR THEORY

In the micropolar theory, the motion of matter is described by a translational velocity, $u_i(\boldsymbol{x}, t)$, and a rotational velocity field, $\omega_i(\boldsymbol{x}, t)$, where $\boldsymbol{x}$ and t denote the spatial position and time, respectively, and i stands for the i^{th} component of each vector and goes from 1 to 3 in 3-D. A second-order tensor, $I_{ij}(\boldsymbol{x}, t)$, the so-called microinertia tensor, is introduced to model particle shape effects, where j goes from 1 to 3 in 3-D.

For the special case of a spin-isotropic micropolar fluid, $I_{ij}(\boldsymbol{x}, t) = I\delta_{ij}$ (δ_{ij} being the Kronecker symbol and I is a constant), the transport equations are given below. The conservation of mass maintains the same form as in classical continuum theory:

$$\frac{\partial \rho}{\partial t} + \frac{\partial \rho u_i}{\partial x_i} = 0 \tag{1}$$

where ρ is the fluid density (Einstein's convention applies here).

The conservation of linear momentum has a similar form to the conversation equation of classical fluids with the only difference that now the second-order tensor, σ^d_{ij} which denotes the viscous part of the stress tensor, $\sigma_{ij} = -p\delta_{ij} + \sigma^d_{ij}$, is asymmetric:

$$\frac{\partial(\rho u_i)}{\partial t} + \frac{\partial(\rho u_j u_i)}{\partial x_j} = -\frac{\partial p}{\partial x_i} + \frac{\partial \sigma^d_{ji}}{\partial x_j} + f^b_i \tag{2}$$

where p and f_i^b are the pressure and the body force per unit volume, respectively. The asymmetry of the stress tensor is due to the different form of the balance of angular momentum:

$$\frac{\partial(\rho I\omega_i)}{\partial t}+\frac{\partial(\rho u_j I\omega_i)}{\partial x_j}=\varepsilon_{ijk}\sigma^d_{jk}+\frac{\partial m_{ji}}{\partial x_j}+T^b_i. \quad (3)$$

The term m_{ij} denotes the so-called moment-stress tensor, which for granular materials is linked to the moments developed at the contacts formed between adjacent particles [2]. The terms T_i^b and ε_{ijk} denote the body moments per unit volume and the permutation symbol, respectively. Finally, the energy balance for micropolar fluids takes the form

$$\begin{aligned}\frac{\partial(\rho e)}{\partial t}+\frac{\partial(\rho u_j e)}{\partial x_j}=-p\frac{\partial u_i}{\partial x_i}+\sigma^d_{ji}\left(\frac{\partial u_i}{\partial x_j}+\varepsilon_{ijk}\omega_k\right)\\ +m_{ji}\frac{\partial \omega_i}{\partial x_j}+\frac{\partial q_i}{\partial x_i}.\end{aligned} \quad (4)$$

where e and q_i are the internal energy and heat flux vector, respectively.

By taking into account that the internal energy can be written in terms of enthalpy, $h=e+p/\rho$, and that the increment of h is written as

$$dh=C_p dT+\frac{1}{\rho}\left(1-\beta T\right)dP \quad (5)$$

where C_p is the heat capacity at constant pressure and β is the thermal expansion coefficient:

$$\beta=-\frac{1}{\rho}\frac{\partial\rho}{\partial T}\bigg|_{\rho}, \quad (6)$$

the conservation of energy can be written in terms of temperature

$$\begin{aligned}C_p\frac{(\partial\rho T)}{\partial t}+C_p\frac{\partial(\rho u_j T)}{\partial x_j}=\beta T\left(\frac{\partial p}{\partial t}+u_i\frac{\partial p}{\partial x_i}\right)\\ +\sigma^d_{ji}\left(\frac{\partial u_i}{\partial x_j}+\varepsilon_{ijk}\omega_k)\right)+m_{ji}\frac{\partial\omega_i}{\partial x_j}\end{aligned} \quad (7)$$

which is the energy equation solved within CS-MICRO.

For spin isotropic micropolar fluids, the pressure and density are related by an equation of the form

$$\rho=p\Phi(I,T) \quad (8)$$

while the viscous part of the stress tensor is related to the velocity and rotational velocity fields by [6]:

$$\begin{aligned}\sigma^d_{ij}=\lambda_v tr\frac{\partial u_k}{\partial x_k}\delta_{ij}+(\mu_v+k_v)\left(\frac{\partial u_j}{\partial x_i}+\varepsilon_{jim}\omega_m\right)\\ +\mu_v\left(\frac{\partial u_i}{\partial x_j}+\varepsilon_{ijm}\omega_m\right).\end{aligned} \quad (9)$$

The viscosity, μ_v, differs from the viscosity of a classical fluid, unless the new viscosity, k_v, is zero. The viscous part of the stress tensor can be related to the classical fluid viscosity, μ, [4]:

$$\sigma^d_{ij}=\lambda_v\frac{\partial u_k}{\partial x_k}\delta_{ij}+2\mu\varepsilon_{ij}-k_v\left(W_{ij}+\varepsilon_{ijm}\omega_m\right) \quad (10)$$

where ε_{ij} and W_{ij} denote the rate of deformation and vorticity tensors:

$$\varepsilon_{ij}=\frac{1}{2}\left(\frac{\partial u_i}{\partial x_j}+\frac{\partial u_j}{\partial x_i}\right)\text{ and }W_{ij}=\frac{1}{2}\left(\frac{\partial u_i}{\partial x_j}-\frac{\partial u_j}{\partial x_i}\right). \quad (11)$$

and the viscosity μ is related to the viscosities μ_v and k_v by the equation $\mu=\mu_v+0.5k_v$.

For spin-isotropic micropolar fluids, the moment stress tensor and heat flux are given by [6]:

$$m_{ij}=\alpha_v\frac{\partial\omega_r}{\partial x_r}\delta_{ij}+\beta_v\frac{\partial\omega_i}{\partial x_j}+\gamma_v\frac{\partial\omega_j}{\partial x_i}+\alpha_T\varepsilon_{ijm}\frac{\partial T}{\partial x_m} \quad (12)$$

and

$$q_k=K\frac{\partial T}{\partial x_k}+\beta_T\varepsilon_{kij}\frac{\partial\omega_i}{\partial x_j}. \quad (13)$$

III. FINITE VOLUME FORMULATIONS FOR THE NUMERICAL MODELING OF MICROPOLAR FLUIDS

A. Discrete transport equations of isotropic micropolar fluids

The discretized transport equations of a micropolar fluid are presented in a symbolic form. Superscripts n and $n+1$ indicate successive time levels, while the superscript $n+\theta$ denotes an intermediate time level where the field values are interpolated linearly from field values at levels n and $n+1$. For an isotropic compressible micropolar fluid, the discretized transport equations can be written as follows:

$$\frac{\rho^{n+1}-\rho^n}{\Delta t}+\nabla_i u_i^{n+1}=0 \quad (14a)$$

$$\begin{aligned}\rho^{n+\theta}\frac{u_i^{n+1}-u_i^n}{\Delta t}&=H\left(u_i^{n+\theta}\right)-\nabla_i p^{n+\theta}\\ &\quad+C^{\omega}\left(\omega_i^{n+\theta}\right)+f_i^{b^{n+\theta}}\end{aligned} \quad (14b)$$

$$\begin{aligned}\rho^{n+\theta}I\frac{\omega_i^{n+1}-\omega_i^n}{\Delta t}&=H\left(\omega_i^{n+\theta}\right)+S^{\omega}\left(\omega_i^{n+\theta}\right)\\ &\quad+C^u\left(u_i^{n+\theta}\right)+C^u(T_i^{n+\theta})\end{aligned} \quad (14c)$$

$$\begin{aligned}\rho^{n+\theta}C_p\frac{T^{n+1}-T^n}{\Delta t}&=H^T\left(T^{n+\theta}\right)+S^{\omega}\left(T^{n+\theta}\right)\\ &\quad+\beta^{n+\theta}T^{n+\theta}\frac{D^F(p^{n+\theta})}{Dt}\\ &\quad+C^{\omega,u}\left(\omega^{n+\theta},u^{n+\theta}\right).\end{aligned} \quad (14d)$$

The operator, H, denotes the finite volume representation of convective and diffusive terms. The operator, ∇_i, denotes gradient calculations within the finite volume framework. The operator, C^l, denotes operations related to the coupling of the transport equation with another field, l. The operator, C^l, may involve the finite volume operators of gradient, curl and divergence. The term, S^k, denotes source-term operators that appear in the transport equation of field k. The operator, D^F/Dt, denotes finite volume operations for the calculation of the material time derivative. In CS_MICRO, the built-in functionalities of Code_Saturne are used to compute the various operators.

A pressure equation can be derived by following the procedure proposed by Issa [9]:

$$\begin{aligned}\nabla_i \nabla_i p^{n+\theta} &= \nabla_i H^*(u_i^{n+\theta}) + \frac{1}{\Delta t}\left(\rho u_i\right) \\ &+ \frac{1}{\Delta t^2}\left(\rho^{n+1} - \rho^n\right) + \nabla_i C^\omega\left(\omega^{n+\theta}\right).\end{aligned} \tag{15}$$

where H^* is a finite volume operator for the convective/diffusive terms where convective terms are expressed in a conservative form.

B. Incompressible micropolar fluid

In CS_MICRO, the coupling of the velocity, rotational velocity and pressure fields is addressed by a sequential process involving a series of correction-prediction steps. Let the superscripts $*$, $**$, $***$ and $****$ denote intermediate values obtained within the splitting process. Terms, $a^{**\theta}$, denote values of the field, a, computed at the intermediate step, $n+\theta$, according to

$$a^{**\theta} = \theta a^{**} + (1-\theta) a^n. \tag{16}$$

(a) Velocity prediction: An estimate of the velocity field, u_i^*, is obtained based on the pressure, $p^{n-1+\theta}$, and rotational velocity, ω^n computed at the previous timestep:

$$\rho \frac{u_i^* - u_i^n}{\Delta t} = H(u_i^{*\theta}) - \nabla_i p^{n+1-\theta} + C^\omega(\omega_i^n). \tag{17}$$

The mass fluxes in operator, H, are computed based on u_i^n. The velocity field, u_i^* does not satisfy the continuity.

(b) Velocity correction due to pressure: A new estimate of the velocity field, u_i^{**}, and a new estimate of the pressure field, p^*, are introduced in order for u_i^{**} to satisfy the continuity equation, i.e., $\nabla_i u_i^{**} = 0$:

$$\rho \frac{u_i^{**} - u_i^n}{\Delta t} = H(u_i^{*\theta}) - \nabla_i p^* + C^\omega(\omega_i^n). \tag{18}$$

By subtracting Eq. (17) from Eq. (18), the corrected velocity is given in an explicit form:

$$u_i^{**} = u_i^* - \frac{\Delta t}{\rho} \nabla_i \left(p^* - p^{n-1+\theta}\right). \tag{19}$$

The corresponding pressure, p^* is obtained by solving a Poisson equation:

$$-\frac{\rho}{\Delta t} \nabla_i u_i^* = -\nabla_i \nabla_i (p^* - p^{n-1+\theta}). \tag{20}$$

New estimates of the mass fluxes at interior and boundary faces are computed based on u_i^{**}.

(c) Rotational velocity prediction: A new estimate of the rotational velocity field, ω_i^* is obtained by solving:

$$\rho I \frac{\omega_i^* - \omega_i^n}{\Delta t} = H(\omega^{*\theta}) + S^\omega(\omega_i^{*\theta}) + C^u(u^{**\theta}). \tag{21}$$

(d) Second prediction of the velocity field: A new estimate of the velocity field, u_i^{***}, is obtained due to the update of the rotational velocity field, ω_i^*:

$$\rho \frac{u_i^{***} - u_i^n}{\Delta t} = H(u_i^{***\theta}) - \nabla_i p^{**} + C^\omega(\omega_i^{*\theta}). \tag{22}$$

For the case of constant viscosities, the operator C_i^ω is divergence free and the new velocity field, u_i^{***}, is solenoidal. In contrast, for non-constant viscosities, the operator $\nabla_i C_i^\omega$ is not zero, and an additional velocity-correction step is required for the velocity field to satisfy the continuity equation.

(e) Second velocity correction due to pressure: For the default treatment of the inhomogeneous case and to ensure that the velocity field will satisfy a priori the continuity equation, new estimates of the velocity, u_i^{****}, and pressure, p^{**}, fields are obtained:

$$-\frac{\rho}{\Delta t} \Delta u_i^{***} = -\nabla_i \nabla_i \left(p^{**} - p^*\right) \tag{23a}$$

$$u_i^{****} = u_i^{***} - \frac{\Delta t}{\rho} \nabla_i \left(p^{**} - p^*\right). \tag{23b}$$

The default strategy of the developed module for addressing the coupling of the transport equations of incompressible isotropic micropolar fluids is comprised of steps (a)-(e). In that case, u_i^{n+1} is set to u_i^{****}. When significant nonlinearities arise, the user has the option to perform multiple iterations consisting of steps (a)-(e) or utilize a slightly modified iterative scheme known as CS_MICRO_SIMPLEX, which involves an additional set of predictions/corrections given by steps (c)-(d)-(e) added after step (e). In that case the velocity field, pressure field and rotational fields at $n+1$ are set accordingly.

It is important to note that step (d) of the default algorithm and the second rotational velocity predictor of the augmented scheme can be replaced with the explicit correction steps. After several trials, we found that replacing Eq. (21) with its explicit counterpart, severe limitations are introduced on the employed timestep. Therefore, the associated transport equations are treated implicitly to remove any timestep restriction.

C. Compressible micropolar fluids

As our primary focus is the modeling of large-scale industrial granular flows, a low Mach number compressible solver is developed. For simplicity, an equation of state given by Eq. (8) is considered. The iterative process within a single time step is outlined next.

(a) Velocity prediction: An estimate of the velocity field, u_i^*, is obtained based on the pressure and rotational velocity fields of the previous step:

$$\rho^n \frac{u_i^* - u_i^n}{\Delta t} = H(u_i^{*\theta}) - \nabla_i p^{n-1+\theta} + C^\omega(\omega^n) \tag{24}$$

The intermediate velocity, u_i^*, does not satisfy the continuity equation.

(b) Velocity correction due to pressure: A new estimate of the velocity field, u_i^{**}, and a new estimate of the pressure field, p^*, are introduced as the velocity field, u_i^{**}, to satisfy the continuity equation:

$$\begin{aligned}u^{**} = \frac{\Delta t}{\rho^{*\theta}} \Bigg[&\left(\rho^{*\theta} - \rho^n\right) \frac{u_i^n}{\Delta t} + \frac{\rho^n u_i^*}{\Delta t} \\ &- \nabla_i (p^* - p^{n-1+\theta}) \Bigg].\end{aligned} \tag{25}$$

and

$$\sum_f m^* = \sum_f \frac{\rho^* \Delta t}{\rho^{*\theta}} S^f \nabla_i (p^* - p^n) - \frac{C_\rho V_c}{\Delta t}\left(p^* - p^n\right) \tag{26}$$

where m^* denotes the mass flux computed at interface f based on u_i^* and ρ^n. The term C_ρ is defined as $\partial\rho/\partial p$. The new density, ρ^*, is computed from the equation of state for (T^n, p^*).

(c) Prediction of the rotational velocity: When dealing with non-uniform thermal viscosities, the moment stress tensor becomes dependent on temperature variations. As a result, we seek an intermediate rotational velocity field, ω_i^*, by setting $u_i^{n+1} \to u_i^{**}$ and $T^{n+1} \to T^n$:

$$\begin{aligned}\rho^{*\theta} I \frac{\omega_i^* - \omega_i^n}{\Delta t} &= H(\omega_i^{*\theta}) + S^\omega(\omega_i^{*\theta}) + C^u(u_i^{**\theta}) \\ &\quad + C^T(T_i^n).\end{aligned} \tag{27}$$

(d) Temperature prediction: An estimate of temperature, T^*, is obtained based on the previous estimates of density, pressure, velocity and rotational velocity $(\rho^*, p^*, u_i^{**}, \omega_i^*)$:

$$\begin{aligned}\rho^* C_p \frac{T^* - T^n}{\Delta} &= H(T_i^{*\theta}) + \beta T^{*\theta} \frac{D^F(p^*)}{Dt} \\ &\quad + C^{\omega,u}(\omega_i^*, u_i^{**}) + S^\omega(T^n)\end{aligned} \tag{28}$$

where the term S^ω denotes source terms that arise due to thermal moments. The non-linear form of $S^\omega(T)$ prevents any implicit treatment of the source term.

(e) Correction of the rotational velocity field due to the temperature field: This correction step is necessary only when dealing with inhomogeneous thermal gyroviscosities. In this case, a new estimate of the rotational velocity field, ω_i^{**} is determined by setting $u_i^{n+1} \to u_i^{**}$ and $T^{n+1} \to T^*$:

$$\begin{aligned}\rho^{*\theta} I \frac{\omega_i^{**} - \omega^*}{\Delta t} &= H(\omega_i^{**\theta}) + C^u(u_i^{**}) \\ &\quad + C^T(T^*) + S^\omega(\omega_i^{**\theta})\end{aligned} \tag{29}$$

(f) Second velocity prediction step: A new estimate of the velocity field, u_i^{***}, is obtained due to the updated rotational velocity field, ω_i^{**}:

$$\rho^{*\theta} \frac{u_i^{***} - u_i^n}{\Delta t} = H(u_i^{***\theta}) - \nabla_i p^* + C^\omega(\omega_i^{**\theta}). \tag{30}$$

(g) Correction of the velocity field and calculation of a new pressure field: As, u_i^{***}, does not satisfy the continuity equation, a new velocity, u_i^{****}, that satisfies the continuity equation, and a new pressure field, p^{**} are obtained:

$$u^{****} = \frac{\Delta t}{\rho^{**\theta}} \left[(\rho^{**\theta} - \rho^{*\theta}) \frac{u_i^n}{\Delta t} + \frac{\rho^{*\theta} u_i^*}{\Delta t} - \nabla_i \left(p^{**} - p^*\right) \right] \tag{31}$$

and

$$\begin{aligned}\frac{\rho^x - \rho^n}{\Delta t} V_c + \sum_f m^* &= \sum_f \frac{\rho^* \Delta t}{\rho^{*\theta}} \nabla_i (p^* - p^n) \\ &\quad - \frac{C_\rho V_c}{\Delta t} \left(p^{**} - p^n\right).\end{aligned} \tag{32}$$

The new density field, ρ^{**} is given by

$$\rho^{**} = p^* \Phi(J, T^*) + C_\rho (p^{**} - p^*) = \rho^x + C_\rho (p^{**} - p^*). \tag{33}$$

For incompressible flows involving non-homogeneous thermo-viscosities, the above iteration strategy is used also to address the thermo-rotational coupling. The only difference between these two iterative strategies is that for the latter the fluid density is constant. In case of constant, thermo-viscosities, the thermal and angular momentum equations are not coupled and the energy equation is treated as an independent equation.

D. *Volume of fluid method*

1) Governing equations: In the volume of fluid method, the two fluids are modeled as a single entity, both obeying the same set of governing equations. The two fluids are identified locally by the void fraction, i.e. the percentage of the unit volume occupied by the given fluid [16]. For an incompressible isotropic micropolar fluid, the governing equations take the form:

$$\frac{\partial u_i}{\partial x_i} = 0 \tag{34a}$$

$$\frac{\partial (\rho u_i)}{\partial t} + \frac{\partial (\rho u_i u_j)}{\partial x_j} = -\frac{\partial p}{\partial x_i} + \frac{\partial \sigma_{ji}}{\partial x_j} + f_i^\sigma \tag{34b}$$

$$\frac{\partial (\rho I \omega_i)}{\partial t} + \frac{\partial (\rho I u_j) \omega_i}{\partial x_j} = \varepsilon_{ijk} \sigma_{jk} + \frac{\partial m_{ji}}{\partial x_j} + T_i^\sigma \tag{34c}$$

where f_i^σ and T_i^σ represent the force and moments resulting from surface tractions and surface moments, respectively. Herein, we assume that f_i^σ and T_i^σ are both zero. The local density, microinertia, viscosities and gyroviscosities are given by:

$$\rho = \varepsilon \rho_1 + (1 - \varepsilon) \rho_2 \tag{35a}$$

$$\rho I = \varepsilon \rho_1 I_1 + (1 - \varepsilon) \rho_2 I_2 \tag{35b}$$

$$\mu_v = \varepsilon \mu_{v_1} + (1 - \varepsilon) \mu_{v_2} \tag{35c}$$

$$k_v = \varepsilon k_{v_1} + (1 - \varepsilon) k_{v_2} \tag{35d}$$

$$\beta_v = \varepsilon \beta_{v_1} + (1 - \varepsilon) \beta_{v_2} \tag{35e}$$

$$\gamma_v = \varepsilon \gamma_{v_1} + (1 - \varepsilon) \gamma_{v_2} \tag{35f}$$

where subsripts 1 and 2 denote different fluids and ε represents the void fraction of fluid 1. In the current iteration, fluid 1 partakes only constant material properties. Lastly, the transport equation of the void fraction is

$$\frac{\partial \varepsilon}{\partial t} + \frac{\partial (\varepsilon u_i)}{\partial x_i} = 0. \tag{36}$$

2) Finite volume discretization: Next, we outline the numerical scheme for solving the transport equations of micropolar fluids with free surfaces.

(a) Volume fraction prediction: The discretized form of the transport equation of the volume fraction is solved first to obtain an estimate of the void fraction field, ε^*:

$$\frac{\varepsilon^* - \varepsilon^n}{\Delta t} + \nabla_i (\varepsilon^{*\theta} u_i^n) = 0. \tag{37}$$

The method proposed in [16] is used to handle the convective term in Eq. (37). Clipping is used to limit the void fraction in the range of $[0, 1]$. Moreover, new estimates of the mass fluxes, m^*, microinertia, I^*, fluid density, ρ^*, and viscosities consistent with the new estimate of the void fraction are obtained based on Eqs. (35).

(b) Velocity prediction: An estimate of the velocity field, u_i^*, is obtained by setting $p^{n+\theta} \to p^n$, $\omega_i^{n+1} \to \omega_i^n$:

$$\rho^{*\theta} \frac{u_i^* - u_i^n}{\Delta t} = H(u_i^{*\theta}) - \nabla_i p^{n-1+\theta} + C^\omega(\omega_i^n). \tag{38}$$

(c) Velocity correction due to pressure: A new estimate of the velocity field, u_i^*, does not satisfy the continuity equation. Hence, new pressure, p^*, and velocity, u_i^{**}, estimates are needed in order for the velocity field to satisfy the continuity constrain at $n{+}1$. The velocity field, u_i^{**}, satisfies the transport equation:

$$\rho^{*\theta} \frac{u_i^{**} - u_i^n}{\Delta t} = H(u_i^{*\theta}) - \nabla_i p^* + C^\omega(\omega_i^n). \tag{39}$$

By taking the difference of the divergence of Eqs. (38) and (39) and taking into account that the velocity field, u_i^{**}, satisfies the continuity equation, we get:

$$-\nabla_i \left[\frac{\Delta t}{\rho^{*\theta}} \nabla_i (p_i^* - p_i^n) \right] = -\nabla_i u_i^*. \tag{40}$$

The mass fluxes are reconstructed from estimates of the density, ρ^*, and velocity, u_i^{**}, fields with the latter to be given by

$$u_i^{**} = u_i^* - \frac{\Delta t}{\rho^{*\theta}} \nabla_i \left(p^* - p^n \right). \tag{41}$$

(d) Prediction of the rotational velocity field: A new estimate of the rotational velocity field, ω_i^*, due to the corrected velocity field, u_i^{**}, is obtained by solving the following transport equation:

$$\rho^{*\theta} I^{*\theta} \frac{\omega_i^* - \omega_i^n}{\Delta t} = H(\omega_i^{*\theta}) + C^u(u_i^{**\theta}) + S^\omega(\omega_i^{*\theta}). \tag{42}$$

(e) Update of the volume fraction: A new estimate of the volume fraction, ε^{**}, is obtained by solving the transport equation

$$\frac{\varepsilon^{**} - \varepsilon^n}{\Delta t} + \nabla_i (\varepsilon^{**\theta} u_i^{**\theta}) = 0. \tag{43}$$

Then, new estimates of the mass flux, fluid density, ρ^{**}, microinertia, I^{**} and fluid viscosities and gyroviscosities are obtained from Eq. (35) based on ε^{**}.

(f) Velocity prediction: A new velocity field, u_i^{***} is obtained by solving implicitly the following transport equation:

$$\rho^{**\theta} \frac{u_i^{***} - u_i^n}{\Delta t} = H(u_i^{***\theta}) - \nabla_i p^* + C^\omega(\omega_i^*). \tag{44}$$

(g) Velocity and pressure correction: As the new prediction velocity field, u_i^{***} does not satisfy the continuity equation, a new estimate of the velocity that satisfy the momentum equation must be obtained. The corrected velocity field, u_i^{****}, satisfies the momentum equation

$$\rho^{**\theta} \frac{u_i^{****} - u_i^n}{\Delta t} = H(u_i^{***\theta}) - \nabla_i p^{**} + C^\omega(\omega_i^{*\theta}). \tag{45}$$

Then, the new pressure field is given by

$$-\nabla_i \left[\frac{\Delta t}{\rho^{**\theta}} \nabla_i (p_i^{**} - p_i^*) \right] = -\nabla_i u_i^{***}. \tag{46}$$

and the corrected velocity is computed explicitly by

$$u_i^{****} = u_i^{***} - \frac{\Delta t}{\rho^{**\theta}} \nabla_i \left(p^{**} - p^n \right). \tag{47}$$

IV. IMPLEMENTATION TO CODE_SATURNE

Code_Saturne is a co-located finite volume method solver that accepts three-dimensional meshes built with any type of cell (tetrahedral, hexahedral, prismatic, pyramidal, polyhedral) and any type of mesh structure (unstructured, block-structured, hybrid). The variables to be solved are stored as field objects (`cs_field_t`) encapsulating the discrete field data and the associated boundary conditions. Code_Saturne comes with build-in functions for calculating the gradient and divergence operators. In addition, Code_Saturne can exploit different partition techniques for domain decomposition. Moreover, the code provides parallel I/O functionality for writing and reading data from disks, functionality that has become increasingly important for codes that use high-end computing resources [7].

A. Structure of the solver

In CS-MICRO, the data fields and solving procedures are organized as follows. The main structure of the developed module is the `cs_micro_system_t` structure, that encapsulates all structures and functions (pointer functions) that are required to solve different sets of transport equations as described in Sec. III. The `cs_micro_fields_t` contains all `cs_fields_t` structures activated by CS-MICRO. Following, the Code_Saturne terminology, the fields are divided into variable and property fields. Variable fields are updated by solving the transport equations, while property fields are computed via an extension of the `cs_xdef_t` mechanism to the finite volume formulation of Code_Saturne which is currently only used in the cdo module. The structure `cs_micro_param_t` contains all the information required for the calculation of the boundary, initial conditions and the calculation of the constitutive laws of micropolar fluids.Due to the similar structure of the discrete linear momentum, angular momentum and energy equations, CS-MICRO exploits `cs_micro_equation_t` structures to form and solve each transport equation. The `cs_micro_equation_t` structure contains all the elements that are necessary to handle the prediction (`cs_micro_predictor_t`) and correction (`cs_micro_correction_t`) steps of each transport equation, see Section III, as well as the procedures to handle the solution of the non-linear equation.

The functions of the predictors of the velocity and rotational velocity are quite similar to the `predv` function of the Navier-Stokes solver of Code_Saturne. The main difference is that in CS-MICRO, the coupling, C, and source S operators are treated by distinct functions. In addition, the convection/diffusion operator, H, is computed in each step of the iterative process used to solve the non-linear system obtained from the discretization of the transport equations.

B. Implementation of the boundary conditions

The mascoscopic fields have to be specified and be consistent with the type of the physical boundaries. CS-MICRO currently supports inlet, outlet, and wall boundary conditions. The information, i.e., boundary type, prescribed values, boundary zones, are stored and handled by the `cs_micro_param_t` structure. The treatment of the boundary conditions within CS-MICRO is similar to the treatment of the boundary conditions in the legacy part of Code_Saturne. Details regarding the treatment of boundary conditions within Code_Saturne can be found in [14].

Next we briefly described the various types of boundary conditions of CS_MICRO

- Inlet: Dirichlet conditions are used for the velocity, rotational velocity and any scalar field while the normal component of the pressure gradient is set to zero.
- Outlet: Homogeneous Neumann conditions are applied to velocity, rotational and scalar fields while the pressure is set to a fixed value, p^{out}, prescribed by the user.
- Wall: For the pressure field, a zero pressure gradient is enforced. For the velocity field, a zero mass flux, is assigned normal to the boundary, while for the tangential component the boundary conditions are of homogeneous Dirichlet type. For scalar fields, Dirichlet and Neumann boundary conditions can be used. For the rotational velocity field, the no-spin or a more general boundary condition that generates some slipping at the interface can also be used. At the same time, the user can use analytic functions to prescribe the tangential component of the velocity field at a given wall.
- Symmetry: For the velocity field, it corresponds to a homogeneous Dirichlet condition for the component normal to the symmetry plane and a homogeneous Neumann condition for the tangential component. For the rotational field, the symmetry condition corresponds to the enforcement of antisymmetric boundary conditions. In particular, a homogeneous Neumann condition is imposed on the component of the rotational velocity field normal to the symmetry plane and a homogeneous Dirichlet for the component tangent to the symmetry plane. For scalar fields, the symmetry conditions correspond to homogeneous Neumann boundary conditions.

The boundary conditions are updated at the beginning of each step based on prescribed values, except for the case of partial-slipping where the boundary condition for the rotational velocity field is recomputed prior to the rotational velocity prediction/correction step. In this case, the rotational velocity is given by

$$\omega_k = \alpha \Omega_k \tag{48}$$

where Ω_k is the vorticity field defined as $\Omega_k = \varepsilon_{ijk} u_{k,j}$, and α a parameter that takes values in the region $[-1/2, 0]$, with the values $-1/2$ and 0 denoting slipping and adherence conditions, respectively.

C. Domain decomposition and MPI parallel communications

CS-MICRO similar to Code_Saturne adapts a brick-type domain decomposition approach for the partition of the simulation domain to multiple subdomains with each cell belonging to a unique domain that is assigned to a unique process. For the domain partition, CS-MICRO can make use of all the available tools included in Code_Saturne, e.g., ParMETIS/METIS, Morton-based based space-filling curves and Hilbrert type curves [7]. Intrasolver communications are treated based on the concept of halo cells, (creating a copy of cells that are adjacent to the sub-domain boundaries). The communications between adjacent processes are handled by the build-in MPI functionalities.

V. BENCHMARK TESTS

Three benchmark cases are considered for the validation of the developed module, including channel flow, Couette flow and two-dimensional cavity flows.

A. Couette flow

As a first verification case, we consider the flow of a micropolar fluid confined between two plates positioned at distance $2\alpha = 1m$ apart. The top wall is moving with velocity, $u_w = 10^{-7} m/s$, while the bottom wall remains stationary. The particles are assumed to adhere to the wall surfaces which at the macroscale is equivalent to the no-spin boundary condition, i.e., $\omega_z(\pm a) = 0$. To account for the special characteristics of the flow, periodic boundary conditions are applied in the $x-$ and $z-$ directions and the simulation domain is reduced into a single column. A grid of 95 elements is used to mesh the fluid column. The viscosity and gyroviscosity of the micropolar fluid are set to $10^{-3} Pa \cdot s$ and $6 \cdot 10^{-7} Pa \cdot m \cdot s$, respectively, while different values of the ratio k_v/μ are considered to assess the coupling of the translational and rotational modes. The outcome of the finite volume simulations are compared with the analytical solution of Cowin [4], see Figs. 1a and 1b. Both figures demonstrate a remarkable agreement between the velocities obtained from the finite volume simulations and those obtained from the analytical solution. In Fig. 2, the non-zero components of the stress tensor obtained from the finite volume simulations is compared with the those obtained from the analytical solution. A remarkable agreement between analytical and finite volume results is observed with the difference between the two stress components to decrease as the ratio, k_v/μ, tends to zero.

B. Channel flow

As a second benchmark case, we consider the flow in a channel driven by a constant pressure gradient while the top and bottom wall, spaced 2α apart remain stationary. For small Reynolds, the particular flow is amenable to an analytical solution [5].

For assessing the performance of the current developments, we model the two-dimensional channel as a one-dimensional column of height $2\alpha = 1.0m$. Periodic boundary conditions are imposed on the faces normal to the flow. Micropolar fluids with μ_v and γ_v coefficients equal to $10^{-4} Pa \cdot s$ and $610^{-5} N \cdot s$ and ratios of k_v/μ_v equal to $\{0, 0.1, 0.5, 1\}$ were considered. The density and microinertia of the various micropolar fluids are set to $1kg/m^3$ and $10^{-6} m^2$, respectively. For all cases, a pressure gradient equal to $3.2 \cdot 10^{-8} Pa/m$ is applied to the fluid. A grid of 19 elements is used to mesh the one-dimensional column.

The horizontal and rotational velocity profiles obtained from the numerical simulations are plotted in Fig. 3. For

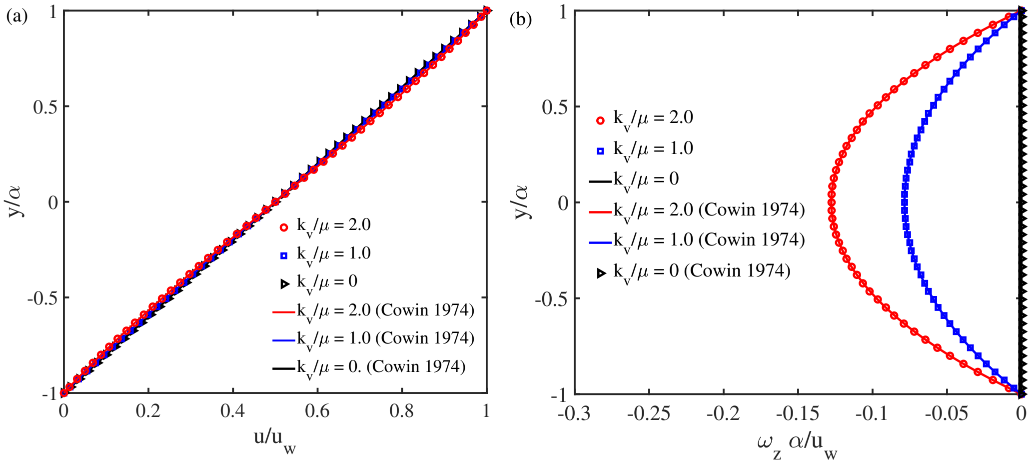

Fig. 1. (a) Velocities and (b) rotational velocities for a Couette flow of micropolar fluids with different values of the ratio k_v/μ. The symbols indicate finite volume data and the lines represent the analytical solution given in Cowin [4].

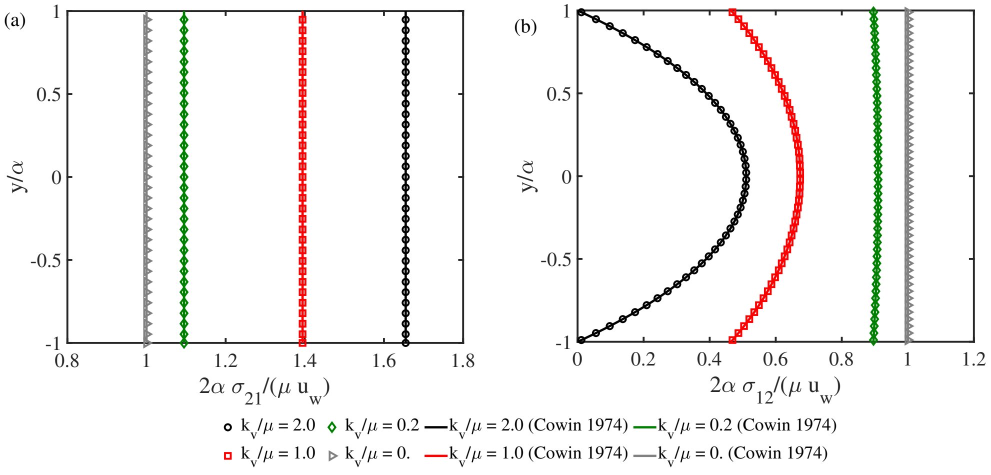

Fig. 2. (a) σ_{21} and σ_{12} for a Couette flow of micropolar fluids with different values of the ratio k_v/μ. The symbols indicate finite volume data and the lines represent the analytical solution given in Cowin [4]).

comparison purposes, the velocity and rotational velocities obtained from the analytical solution are also included in the figure. A remarkably good agreement between the analytically and numerically obtained velocity profiles is observed independently of the ratio k_v/μ_v. Both methods indicate that micropolar fluids experience a "stiffer" response than classical fluids accompanied by larger values of $\omega_z\alpha/u_c$ as the ratio k_v/μ_v increases. In addition, the location of the maximum rotational velocity moves towards the walls as the ratio k_v/μ_v increases.

For the further evaluation of the developed module, we consider the flow of a micropolar fluid in a channel of length $60m$ and height $2m$. At the inlet, a constant velocity u_o of $10^{-6}m/s$ and a zero rotational velocity are prescribed, while at the outlet, Neumann-type boundary conditions are set for both the translational and rotational velocities. The no-slip and no-spin boundary conditions are enforced at the top at bottom walls. We consider two micropolar fluids with $\mu_v = 510^{-4}Pa \cdot s$ and k_v/μ_v ratios of 0 and 2, respectively. For both fluids, the gyrovisocsity coefficients are set to $610^{-7}N \cdot s$ while the fluid density and microinertia are equal to $1kg/m^3$ and $3 \cdot 10^{-10}m^2$, respectively. Due to the specific flow characteristics, we will refer to the micropolar fluid with a $k_v/\mu_v = 0$ as classical fluid, while the micropolar fluid with the ratio $k_v/\mu_v = 2$ is referred as micropolar fluid. A structured grid of 24000 cells is used to mesh the two-dimensional channel. For the micropolar fluid, Poiseuille flow conditions (constant pressure gradient and parabolic velocity profile) are et at a distance $2.75m$ from the inlet, while for the classical fluid, Poiseuille flow conditions were developed at a distance $2.85m$ from the inlet. The measured pressure gradients were $3.099 \cdot 10^{-9}$ for the micropolar fluid and $1.5 \cdot 10^{-9}$ for the classical fluid. The horizontal velocity and rotational velocity profiles found at a distance of $50m$ from the inlet are compared with the profiles obtained from the analytical solution for the uniform pressure gradients reported

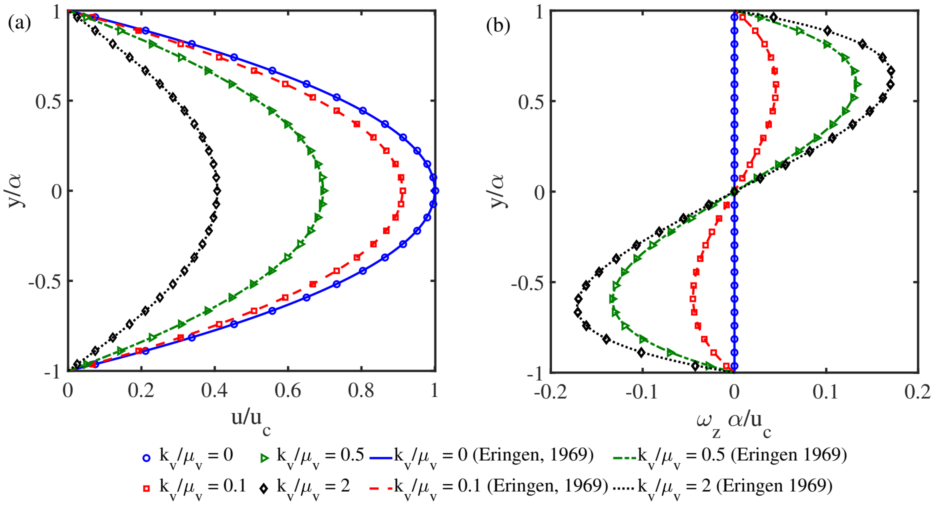

Fig. 3. (a) Velocities and rotational velocities for a Poisseuille flow of micropolar fluids with different values of the ratio k_v/μ_v. Symbols indicate finite volume data for a one-dimensional mesh of grid size $\Delta x = 1/19$. Lines represent the analytical solution given by Eringen [5].

for each case. An excellent agreement between numerical and analytically obtained profiles is observed, Fig. 4.

C. *Cavity flows*

As a third verification case, we consider lid cavity flows which have been widely used in the validation of CFD solvers [18, 17]. Specifically, a square cavity of height $H = 1m$ is considered. A uniform mesh of 125×125 is used. The top wall moves with a horizontal velocity, $u_o = 0.01 m/s$, while the other walls remain stationary. For the rotational motion of the fluids, the no-spin boundary condition is imposed at the four walls. Periodic conditions are considered for the out-of-plane motion.

For verification purposes, we consider lid-driven cavity flows with a $Re_{\mu_v} = \rho u_o H/\mu_v$ equal to 1000. Two micropolar fluids with k_v/μ_v equal to 0 and 5, respectively are considered. Following [17], the gyroviscosities, γ_v, and β_v are set to $(\mu_v + k_v/2)$ and zero respectively, i.e., $I = 1$. The velocity profiles obtained from the finite volume simulations are compared with the velocity profiles obtained from the finite difference simulations of [17] for $k_v/\mu_v = 5$, and the velocity profiles given in [8] for the Newtonian case, $k_v/\mu_v = 0$ (Fig. 5). The comparison of the velocity profiles shows a remarkable agreement between the velocities obtained from the finite volume and finite difference simulations.

VI. PARALLEL PERFORMANCE

To assess the parallel performance of CS_MICRO as a standalone package, the flow of a micropolar fluid confined in a three-dimensional cavity of dimensions of $(10m, 10m, 5m)$ is chosen. In this setup, the top wall moves with a horizontal velocity, $u_o = 0.01 m/s$. The Reynolds number, $Re = \rho u_o L/(\mu_v + 0.5 k_v)$ is set to 1000, where $L = 10$. The ratio, k_v/μ_v, and the microinertia, I, are equal to 1 and $10^{-4} m^2$, respectively. The no-slip and no-spin boundary conditions are enforced at the cavity walls.

Structured and unstructured grids of different sizes are used to mesh the three-dimensional cavity. The structured meshes consist of 32 and 256 million elements, respectively, both generated using Code_Saturne's mesh multiplication capabilities from an initial structured mesh of 0.5 million hexahedral elements. Additionaly, three unstructured meshes of 11, 88 and 704 million tetrahedral elements respectively, are used to further assess the parallel performance of the developed module. The last two meshes are obtained from the 11 million element mesh using Code_Saturne's mesh multiplication capabilities.

The benchmark simulations are carried out on the UK national supercomputing service ARCHER2 which is a HPE Cray supercomputing system with dual AMD EPYC$^{\text{TM}}$ 7742 type 64-core processors. The parallel performance of the developed module is analyzed based on the speed-up ratio which is defined as the ratio of the time required by the minimum number of fully populated nodes, n_{min} (or $128 \times n_{min}$ processes) to run for 50 steps to the runtime taken by n nodes, $128 \times n$ processes, for the same number of steps. The minimum number of nodes for each individual mesh is identified based on memory considerations. Using a memory logger tool (memlog), we estimate that the maximum number of cells that can be handled by each process is around 1 million cells. For the compressible solver, this number decreases due to the introduction of additional fields.

The speed-up of CS_MICRO for the meshes employed in the benchmark simulations is presented in Fig. 6. According to Fig. 6, CS_MICRO retains the excellent parallel performance of Code_Saturne up to around 10000 cells per process (MPI task). After this point, the runtime reaches a plateau, not shown in the figure. A detailed profiling of the CS_MICRO reveals that the bottleneck in the parallel performance is related to the efficiency of the parallellized linear solvers that are used in the solution of the linearized transport equations within each iteration. The parallel performance of the linear solvers is limited due to global MPI communications that take over.

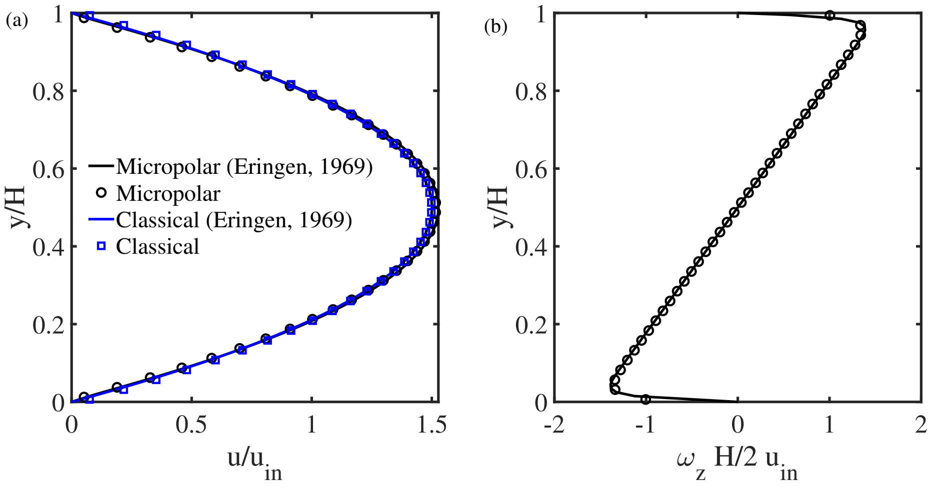

Fig. 4. (a) Velocities and (b) rotational velocities along the vertical axis at $x = 50m$ where Poiseuille flow conditions are established. Symbols indicate finite volume data while lines represent the analytical solution given by Eringen [5]

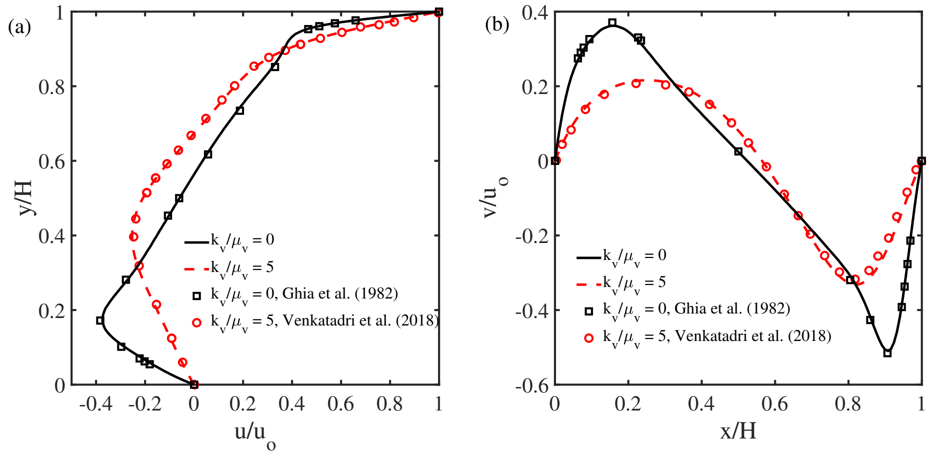

Fig. 5. Lid-driven cavity flow. Plots of (a) the u and (b) v components of the velocity field along a vertical and a horizontal line passing from the geometric center of the cavity, respectively for $Re_{\mu_v} = 1000$ and $k_v/\mu_v = 0$ and 5.

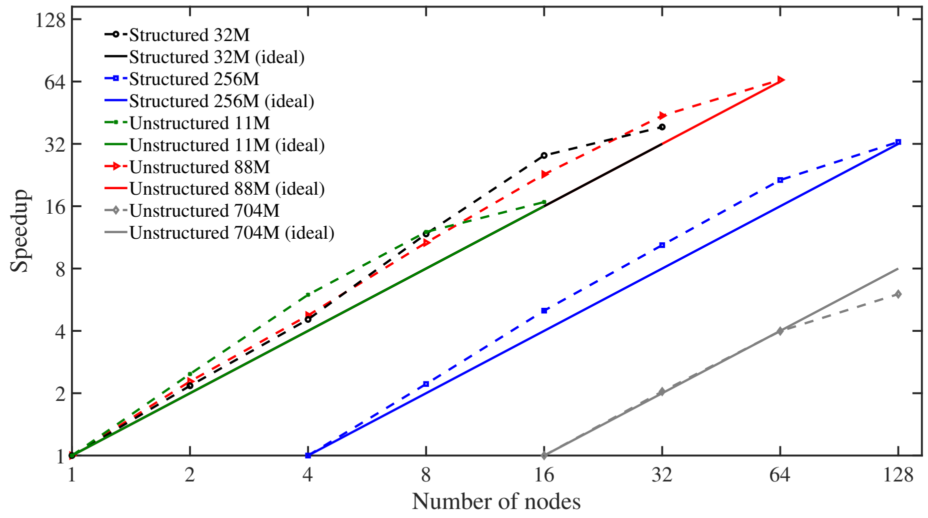

Fig. 6. Speed up reported for four different meshes of tetrahedra and hexahedra elements.

For instance, when running a simulation with the unstructured mesh of 88 million cells on 64 nodes, about 75% of the total runtime is spend in the linear solvers. In contrast, when the same simulation is run on two nodes, the time spent in the linear solver decreases to 32% of the total time.

VII. CONCLUSIONS

An open-source finite volume solver of the transport equations of isotropic micropolar fluids is developed within the Code_Saturne framework. The developed module is validated using numerically or analytically obtained benchmark cases for classical and micropolar fluids. The results are in excellent agreement with either numerically or analytically obtained results.

The developed module utilizes all the features of Code_Saturne that renders Code_Saturne an excellent platform for the modeling of large-scale industrial applications. Moreover, CS-MICRO inherits all the pre- and post-process capabilities of Code_Saturne.

ACKNOWLEDGMENT

This work was funded under the embedded CSE programme of the ARCHER2 UK National Supercomputing Service (http://www.archer2.ac.uk)

REFERENCES

[1] F. Archambeau, N. Méchitoua, and M. Sakiz. Code saturne: A finite volume code for the computation of turbulent incompressible flows-industrial applications. *Int. J. Finite Vol.*, 1(1):http–www, 2004.

[2] C. S. Chang and C. L. Liao. Constitutive relation for a particulate medium with the effect of particle rotation. *Int. J. of Solids Struct.*, 26(4):437–453, 1990.

[3] E. Cosserat and F. Cosserat. *Theorie des corps deformables*. Hermann, Paris, France, 1909.

[4] S. C. Cowin. The theory of polar fluids. *Adv. Appl. Mech.*, 14:279–347, 1974.

[5] A. C. Eringen. Mechanics of micropolar continua. In M. Reiner, editor, *Contributions to Mechanics*, pages 23–40. Elsevier, 1969.

[6] A. C. Eringen. *Microcontinuum field theories: II. Fluent media*. Springer Science & Business Media, 1998.

[7] Y. Fournier, J. Bonelle, C. Moulinec, Z. Shang, A. G. Sunderland, and J. C. Uribe. Optimizing code_saturne computations on petascale systems. *Comput. Fluids*, 45(1):103–108, 2011.

[8] U. Ghia, K. N. Ghia, and C. Shin. High-Re solutions for incompressible flow using the navier-stokes equations and a multigrid method. *J. Comput. Phys*, 48(3):387–411, 1982.

[9] R. I. Issa. Solution of the implicitly discretised fluid flow equations by operator-splitting. *J. Comput. Phys.*, 62(1):40–65, 1986.

[10] E. Karvelas, G. Sofiadis, T. Papathanasiou, and I. Sarris. Effect of micropolar fluid properties on the blood flow in a human carotid model. *Fluids*, 5(3):125, 2020.

[11] K. S. Mekheimer and M. E. Kot. The micropolar fluid model for blood flow through a tapered artery with a stenosis. *Acta Mech. Sin.*, 24(6):637–644, 2008.

[12] N. Mitarai, H. Hayakawa, and H. Nakanishi. Collisional granular flow as a micropolar fluid. *Phys. Rev. Lett.*, 88(17):174301, 2002.

[13] L. S. Mohan, P. R. Nott, and K. K. Rao. A frictional cosserat model for the flow of granular materials through a vertical channel. *Acta Mech.*, 138(1):75–96, 1999.

[14] F. D. D. Single Phase Thermal-Hydraulics Group. code_saturne 8.0 theory guide. Technical report, EDF, 2023.

[15] G. Sofiadis and I. Sarris. Reynolds number effect of the turbulent micropolar channel flow. *Phys. Fluids*, 34(7), 2022.

[16] O. Ubbink and R. I. Issa. A method for capturing sharp fluid interfaces on arbitrary meshes. *J. Comput. Phys.*, 153(1):26–50, 1999.

[17] K. Venkatadri, S. Maheswari, C. V. Lakshmi, and V. R. Prasad. Numerical simulation of lid-driven cavity flow of micropolar fluid. In *IOP Conference Series: Materials Science and Engineering*, volume 402, page 012168. IOP Publishing, 2018.

[18] L. Zhu, Z. Guo, and K. Xu. Discrete unified gas kinetic scheme on unstructured meshes. *Comput. Fluids*, 127:211–225, 2016.